ELSEVIER

Contents lists available at ScienceDirect

Advances in Water Resources

journal homepage: www.elsevier.com/locate/advwatres



A new sequential procedure for hydraulic tomographic inversion



S. Jiménez, R. Brauchler, P. Bayer*

Federal Institute of Technology, ETH Zurich, Department of Earth Sciences, Sonneggstrasse 5, CH-8092 Zurich, Switzerland

ARTICLE INFO

Article history:
Received 14 January 2013
Received in revised form 30 September 2013
Accepted 2 October 2013
Available online 10 October 2013

Keywords: Hydraulic tomography Travel time inversion Pilot points Aquifer analogue Graph theory

ABSTRACT

We present a novel hydraulic tomography procedure, which is based on a travel-time based inversion and application of pilot points. The travel-time based inversion allows for the reconstruction of a diffusivity distribution, which displays the dominant structural elements of a heterogeneous aquifer. This information is used to guide pilot point based inversion of hydraulic conductivity distribution. We utilize the diffusivity distribution to optimize the spatial positions of the pilot points and the relationships among them. For the implementation of the relationships, graph theory is applied. The associated high-computational effort was encountered with subspace regularization and parallel computing. The developed inverse methodology was successfully applied to a three-dimensional sedimentary aquifer analogue. The validation shows that the sequential procedure strongly improves the misfit between predicted and true pressure response in comparison to the results, only when travel-time inversion is employed.

1. Introduction

Hydraulic tomography (HT) has evolved as a promising technique for examining spatially heterogeneous hydraulic conductivity and specific storage in aquifers. The method allows for the reconstruction of hydraulic parameter distributions in two and three dimensions with a resolution and accuracy superior to that possible with type curve analysis based on a homogeneous parameter distribution [1]. A comparison between different heterogeneity modeling approaches and HT can be found in Berg and Illman [2] and Illman et al. [3,4]. The origin of HT is in medical applications [5] and was introduced in hydrogeology by Bohling [6], Tosaka et al. [7] and Gottlieb and Dietrich [8], among others. While in medicine X-rays are used to image sections of a body, in our discipline, hydraulic pulses are applied to characterize the subsurface [1,9–12]. These pulses commonly stem from sequential pumping or injection at a well, which is divided in different vertical sections by a packer. During the perturbation from each section, the hydraulic pressure response of the aquifer is monitored, typically at other observation wells that act as receivers. The recorded response is controlled by the hydraulic properties of the aquifer, and so can be deployed to reconstruct subsurface heterogeneity through an inversion procedure. The potential of HT was successfully demonstrated on different scales and for different aquifer types, e.g. on laboratory scale utilizing sandbox experiments [2,3,13-18], investigating unconsolidated aquifers on field scale [1,19–21], as well as in laboratory and field studies in fractured rocks [10,22–24].

Bohling and Butler [25] offered a cautionary note to illustrate the inherent non-uniqueness of hydraulic tomography. It is emphasized that it is possible to obtain different realizations of the aguifer parameters, using HT techniques, which vary from each other and from reality, even when high-quality drawdown data is available. This highlights an eminent challenge for many inversion procedures in hydrogeology dealing with spatial heterogeneity. Often, some form of regularization is introduced in order to simplify the tomographic equation system. Cardiff and Barrash [26] give an overview of the different hydraulic tomographic inversion methods and the applied regularization techniques. The vast majority of proposed HT studies utilize geostatistical a priori information (regularizers), such as correlation length and variance of the parameter space. Lavenue and de Marsily [27] and Vesselinov et al. [28,29] applied pilot-point based geostatistical inverse methods for the joint inversion of hydraulic and pneumatic tests in fractured systems. Castagna et al. [30,31] applied pilot points for joint estimation of transmissivity and storativity in a fractured system. They implemented pilot points in a Bayesian inversion scheme and estimated transmissivity and storativity for each pilot point, as well as the integral scale, mean and variance within the model domain. Bohling and Butler [25] used a pilot-point based inversion approach to illustrate the non-uniqueness of HT. Thereby, the dimension of the parameter space was reduced by more than one order of magnitude from 5202 (storage and transmissivity estimates) to 354. For the reconstruction of the parameter space between the pilot points, a thin-plane spline interpolation function was applied. Aside from geostatistical a priori information, several

^{*} Corresponding author. Tel.: +44 41 633 6829. E-mail address: bayer@erdw.ethz.ch (P. Bayer).

authors have included independent geological information, such as flow meter data [32], self-potential signals [33] and structural information derived from georadar data [34] to constrain the inversion.

The multiplicity of solutions that are generated by HT calls for a rigorous evaluation of reconstructed tomograms. For this purpose, a first order estimation of the parameter covariance [35], Monte Carlo analysis [25,30], or pressure response curves not used for the inversion (e.g. [14,36]), can be employed. Another possibility is to exploit results from other field investigation techniques, e.g. from multi-level slug testing [37], direct-push logging [19] or geophysical investigations [38]. However, the use of independently collected data to validate HT results can be a challenge, for instance, in the case of different observation scale and mismatch in the resolution [38].

In this study, we present a novel inversion procedure, which combines a travel-time based inversion scheme [39] with a subsequent pilot-point based inversion step [27]. The motivation of combining these two methods is to exploit the high structural resolution of the calculation-efficient travel-time based inversion approach in order to tune the pilot-point based inversion approach. This involves enhanced regularization, minimization of the number of pilot points and optimizing their spatial position. The travel-time based inversion scheme is based on the transformation of the flow equation into a form of the eikonal equation using an asymptotic approach [39]. We solve the travel-time based inverse problem utilizing computationally efficient eikonal solver. The reconstructed diffusivity distribution, together with a calculated null-space energy map, is utilized to assign pilot points and for tuning the regularization during hydraulic conductivity estimation. The pilot-point based inversion method was selected because it represents a hybrid method with deterministic and stochastic components. Even more important, it offers the possibility of easily including a priori information.

In the following, the sequential steps of the developed inversion scheme are individually described. Then, a numerical case study is presented, which is a tomographic suite of pressure response curves simulated on a three-dimensional (3-D) aquifer analogue. The full procedure is applied to this case study and the obtained hydraulic conductivity distribution of the inspected aquifer is validated.

2. Methodology

2.1. Workflow of sequential HT inversion procedure

The full inversion procedure consists of four major components, which are depicted in Fig. 1 and described in detail below. The database gathered and utilized for the HT analysis is the pumping schedule at a source well and the associated responses recorded at close-by receiver well(s). The diffusivity is estimated by traveltime inversion of early travel-time diagnostics (see, e.g. [40]). The diffusivity tomogram obtained for a specific vertical cross-section between source and receiver is transformed into a structure map by clustering and by means of the estimated null-space energy maps. The structural map serves as a basis for assigning pilot points and for tuning the regularization during the subsequent hydraulic conductivity estimation.

2.2. Hydraulic experiment

In order to create a hydraulic tomography reconstruction, the necessary information must be collected in the form of pressure response curves. Different techniques can be used to induce a perturbation at different depths in a borehole and to record the pressure

responses in multiple observation points. Pumping and slug tests are the most common way to create such perturbation in the aquifer, using a cross-well setup. Depending on the number and disposition of the source and receivers, two-dimensional (2-D) or 3-D reconstructions will be possible. Recent developments in well installation, e.g. direct-push technology [41], and equipment such as portable, modular packer systems [42], facilitate highly time-efficient hydraulic tomography tests in shallow aquifers. However, there is still a need for developing more advanced multi-packer, data acquisition and semi-automatic systems for test initiation.

Numerical simulations are often a cost effective alternative to field campaigns to develop and evaluate new investigation techniques, such as a new hydraulic tomographic inversion scheme. These numerical experiments provide us with the possibility to compare the reconstructed parameter field with the "true" parameter distribution (*K*-field), which again allows for a rigorous validation. Aquifer analogues are especially well suited because they realistically imitate geological and hydraulic heterogeneity.

2.3. Estimation of spatial diffusivity distribution

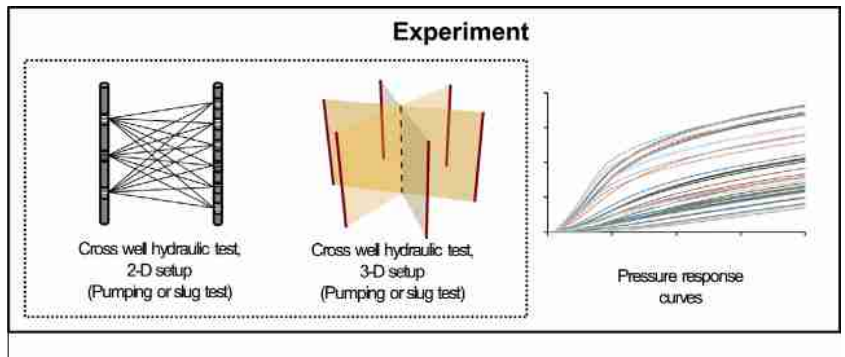
The travel-time based inversion approach that was proposed by Vasco et al. [39] is oriented at a fundamental procedure from seismic ray tomography, which is adopted in HT to reconstruct spatially variable diffusivity. The relationship between the arrival time of a hydraulic signal and diffusivity, D, is expressed by a line integral [39]:

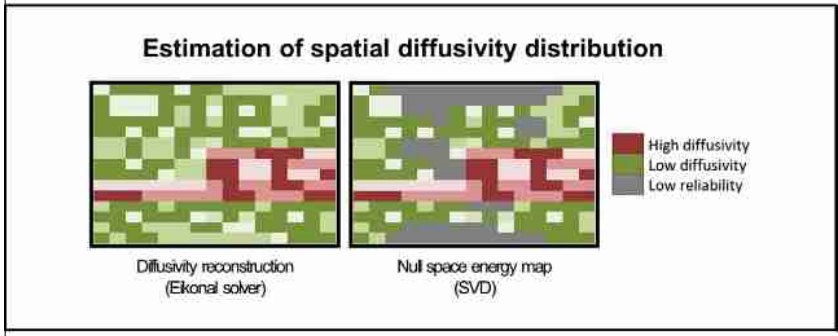
$$\sqrt{t_{peak}(x_2)} = \frac{1}{\sqrt{6}} \int_{x_1}^{x_2} \frac{ds}{\sqrt{D(s)}}$$
 (1)

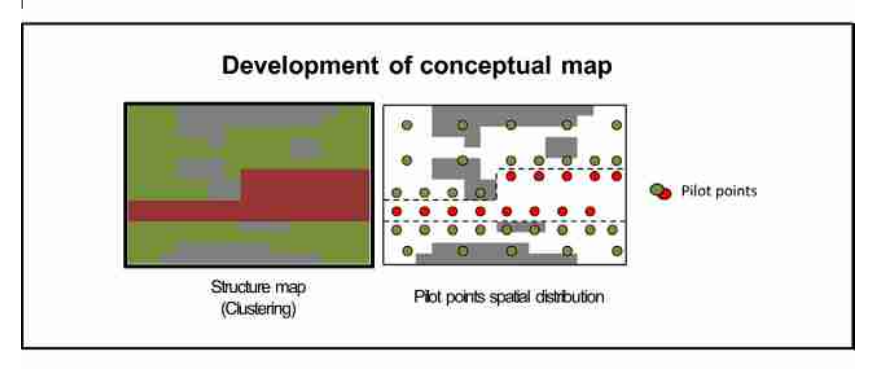
where t_{peak} is the travel time of the peak of a Dirac signal from the source (position x_1) to the receiver (x_2).

By differentiation of transient head data measured at the receiver(s), the inversion scheme is also applicable to experiments with constant pumping rates over a given short period of time (e.g. [39,40]). Moreover, Brauchler et al. [43] demonstrated that instead of the peak travel time, inspection of an earlier time behavior of the received hydraulic signal is preferable to analyze preferential flow paths. The latter delineate connected high conductivity zones, and their localization is of particular interest for prediction of flow and transport in heterogeneous aquifers. In our study, we follow the suggestion of Hu et al. [40], and exclusively inspect the time at which the pressure pulse rises to 10% of its peak value, that is, the t-10% diagnostic. Hu et al. [40] showed that limiting the angle between source and receiver is recommendable in many aquifers, where horizontal and layered structures dominate. This way, focus is set on source-receiver combinations that follow the expected structures, rather than providing an integral signal from different layers. For more details on the implementation of the angle constraint and travel-time diagnostics the reader is referred to [10,40,43]. In our study, diffusivity is reconstructed by utilizing the eikonal solver CAT3D, which is based on the SIRT (Simultaneous Iterative Reconstruction Technique) and ray tracing algorithm originally developed to determine seismic velocities. The used curved ray tracing algorithm is described in great detail in Brauchler et al. [44]. The complete inversion procedure delivers a pixel-based diffusivity tomogram for a given source-receiver combination within a few seconds of computation.

Due to sparse data and spatially varying data density, some parts of the imaged section are more reliable than those of others. There are several criteria to quantify uncertainty and reliability of travel-time inversion, such as ray density and angular coverage. The generation of a null space energy map is a robust way to rank the reliability of the different pixels in a tomogram. In the following, a short description of the calculation of the null-space energy







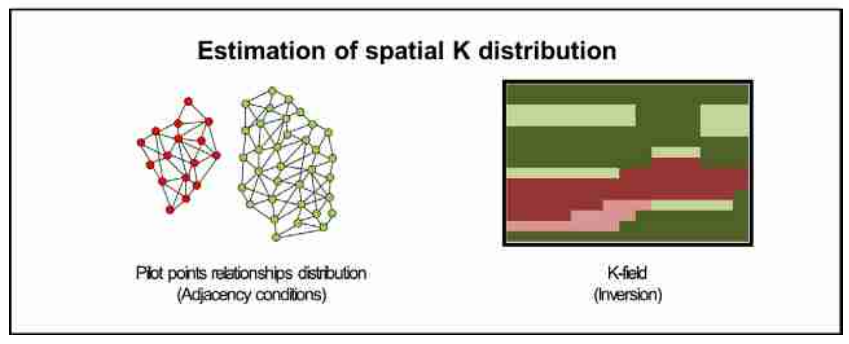


Fig. 1. Workflow corresponding to the main steps, presenting the new inversion framework, from data collection, hydraulic tomography reconstruction, to the final pilot point inversion.

map, which is based on the work of Böhm and Vesnaver [45], is given. The null space map method comprises a singular value decomposition (SVD) of the tomographic matrix (**A**), where A_{ij} of the matrix **A** are the lengths of the i_{th} trajectory path in the j_{th} pixel. This matrix can be factorized into three components by applying SVD:

$$\mathbf{A} = \mathbf{UWV}^{\mathbf{T}} \tag{2}$$

The square matrices \boldsymbol{U} and \boldsymbol{V} are orthonormal.

The elements w_{ii} of the diagonal matrix **W** are the singular values of **A** and correspond to the square root of the eigenvalues of transpose **A** times **A**. The reliability of the estimated parameters

by HT inversion can be evaluated utilizing the singular values w_{ii} . Small singular values show potential instabilities of the inversion process. We reorganized the singular values according to their numerical value. Taking into account that the columns of \mathbf{V} of the matrix decomposition (Eq. (2)) display an orthonormal basis of the model space, a local reliability, R_i , of each pixel can be defined. Therefore, the squared elements v_i of \mathbf{V} are summed up as follows:

$$R_i = \sum_i v_i^2 \tag{3}$$

Note, the summation of the elements is equal to one if the index *i* covers the whole model space. By introducing a threshold to separate large and small singular values we can use the summation

displayed in Eq. (3) to assign each pixel a value ranging from 0 to 1. Pixels associated with high values of null space energy reflect high uncertainty and vice versa. Pixels with a high uncertainty are neglected for the subsequent development of the conceptual maps.

2.4. Development of conceptual maps

Travel-time inversion between a source and receiver well delivers a diffusivity section, in the following called D-tomogram. Diffusivity is defined as the ratio between hydraulic conductivity, K, and specific storage, S_s. Therefore, it can be assumed that a D-tomogram carries valuable structural information with respect to the *K*-distribution, because the *K*-distribution typically shows a higher variability than the S_s-distribution in the subsurface. However, sparse data, spatially varying data density, as well as measurement errors, can lead to inaccurate reconstruction. Hence, clustering is suggested by Brauchler et al. [1], and this yields a zoned diffusivity image, for which the respective K-values are then calibrated. This approach supposes that the "true" parameter distribution is better described as discrete rather than as continuously varying. By crude clustering, however, information is lost and the determined static structures will strongly depend on the chosen clustering technique.

As an alternative, we utilize clustering to obtain zonal images that serve as basic conceptual schemes. Clustered zones represent initial estimations of facies distribution, and these will be adjusted during the *K*-field estimation step. That means the boundaries are not fixed as well as the homogeneous *K*-field distribution of each zone is allowed to change into a heterogeneous *K*-field during inversion

As standard method, here k-means clustering is applied without any spatial adjacency [46]. The number of clusters was derived from a dendrogram based on hierarchical clustering. In hierarchical clustering e.g. [47,48] the most similar observations, in our case values of D, are taken to define a cluster. Successively, the next most similar observations are connected to the initially defined clusters. This procedure is repeated until all values of D are connected. The distances between the clusters are visualized in a dendrogram and are utilized to determine an optimum cluster number for the k-means clustering.

An illustrative example of a structure map is shown in Fig. 1. The structure map indicates that only those pixels are clustered where sufficient information is available, that is, where the null space energy is below a given threshold. This threshold, however, is not well defined and is case-specific depending on the number of available trajectories and the spatial discretization of the domain. The cells characterized by a low reliability, i.e. high null space energy, are not considered during the clustering step. After the clustering step, these "gap cells" are assigned to the respective clusters based on the cluster association of their neighboring cells. In Fig. 1, the pixels with a low reliability are displayed in grey.

The transient hydraulic head response carries more information than the 10% travel-time diagnostic utilized for the travel-time inversion. Since the influence of aquifer storativity diminishes with later times [49,50], information on *K*-values is ideally derived from the later part of the transient pressure responses. This is also considered in our procedure. For the estimation of *K*-values, pilot points are used [51–53]. The underlying concept is that the *K*-field is calibrated at given points, and then a spatial interpolator is employed to assign the parameter values to the rest of the aquifer [54]. In line with Doherty et al. [55,56] and others [57–60], we chose ordinary kriging for interpolation between the pilot points.

A crucial and critical aspect is the positioning of the pilot points. Doherty [61] proposes placing points at measurements locations, close to the boundaries of the model domain, and oriented at the head gradient. Pilot points should also be positioned where they

are most sensitive to the model predictions [62]. In areas where a high hydraulic property change is observed, the density of the pilot points should be greater than in areas of small variation [63]. Within our HT framework, the information gained from traveltime inversion is used to guide the allocation of pilot points. We utilize a finite element mesh generator (free triangular) in order to design a mesh for each cluster. To each node of the mesh a pilot point is assigned. This procedure leads to a refinement of the pilot point distribution at the interface between two clusters, representing initial estimations of facies boundaries. Once the spatial position of each pilot point is determined, this position is kept constant during the inversion. The resolution, that is, number of elements of the designed mesh is a compromise between required resolution, available observations, in our case number of transient pressure responses and calculation demand. Note that the generated mesh is not identical to the mesh we used for the forward simulation step of the pilot-point based inversion discussed in the next section.

2.5. Estimation of spatial hydraulic conductivity distribution

The last step is the calibration of the K-distribution by assignment of facies-specific K values to each pilot point and flexible adjustment of facies boundaries. The objective function Φ , of the parameter estimation problem thus combines two goals. One is to adjust the K-field so that the receiver response is matched by the flow model prediction, and the other is to comply with the structures anticipated by diffusivity clustering:

$$\min \Phi = \Phi_m + \Phi_r \tag{4}$$

The first goal is expressed by minimization of Φ_m . It represents the minimization of residuals when calibrating the late head responses at the receiver(s), which are computed by a numerical groundwater flow model (e.g. [55]). Φ_m is called model function in the following. The second goal is to minimize the regularization function, Φ_r , which tries to keep the structure derived from the diffusivity–clustering step. In order to minimize the model function Φ_m subject to the regularization function, Φ_r , which can be seen as a constrain, the Lagrange multiplier method is applied. The optimization problem is then reduced to find a point in the parameter space, where the gradient of model function and regularization function are parallel:

$$\nabla \Phi_m = \lambda \nabla \Phi_r,\tag{5}$$

where λ is a constant, which expresses the difference in the magnitudes of the gradient vectors.

The rationale of the preceding diffusivity–clustering step was to obtain facies-based zones rather than an unrealistic scattered image. Similarly, pilot points application is often combined with a regularization step [58,64]. This is applied to create geologically plausible zoned *K*-fields, and this way, by increasing the uniqueness of the solution, to stabilize the inverse problem. There exist several regularization methods [65], from which Tikhonov and subspace methods are selected for our procedure. In detail, a facies-based, smoothing Tikhonov regularization method is employed. It includes a set of rules that will be explained in the following.

We need a regularization technique that maintains spatial continuity of zones consistent with the diffusivity tomograms. However, the resolution by travel-time inversion is limited and small-scale heterogeneities may exist, which are blurred in the tomograms. Therefore, regularization should find a balance between maintaining extensive zones and flexible identification of potentially existing small-scale heterogeneities. For these purposes, the spatial relationships between the pilot points are examined by utilization of graph theory. The use of graph theory

to examine adjacency conditions has also been suggested by [66], who introduced a spectral domain parameterization for multiscale aquifer heterogeneity zonation. In our methodology, the pilot points are interpreted as the vertices of a graph, and the connections between the pilot points, the edges, are given by their mutual relationship. Initially, before the calibration is conducted, each pair of pilot points is examined and an adjacency matrix is developed:

$$\begin{pmatrix} 0 & \dots & a_{ij} \\ \vdots & \ddots & \vdots \\ a_{ij} & \dots & 0 \end{pmatrix} \leftarrow C(p_i, p_j) = \begin{cases} 1, conditions satisfied \\ 0, otherwise \end{cases}$$
 (6)

where $i = j = 1, \dots$, total number of pilot points, a_{ij} is a boolean *indicator*, p denotes pilot points with coordinates and cluster categories.

We define three conditions which have to be fulfilled so that two pilot points are allowed to connect (Fig. 2): (i) both pilot points pertain to the same cluster (Fig. 2a). (ii) The distance d between the pilot points is smaller than the average length of the cluster in horizontal direction, r (Fig. 2b). (iii) There must be no other pilot points from a different cluster within a space of influence, defined by the angle α and the distance d between two selected points; this is necessary to account for cluster boundaries (Fig. 2c and d). For calculating the angle α we select one pilot point A, and the two closest pilot points B and C associated with the same cluster. Then we construct a triangle ABC and calculate the angle between the sides AB and AC. This is done for all possible pilot point combinations and finally the angle α is specified by the arithmetic mean of all calculated angles.

The adjacency matrix (Eq. (6)) determines if there is connectivity between two pilot points and is used to calculate the regularization function Φ_r . Therefore, the adjacency matrix \mathbf{C} is multiplied with vector \mathbf{p} , containing the K-value of each pilot point for a given iteration step. By squaring the product, we receive:

$$\mathbf{M}(\mathbf{p}) = (\mathbf{C} \cdot \mathbf{p})^2 \tag{7}$$

Note, the matrix \mathbf{C} is constant during the whole inversion and the vector p is updated after each iteration step. The squared regularization values $\mathbf{M}(\mathbf{p})$ (Eq. (7)) are utilized to define the regularization function Φ_{r_0}

$$\Phi_r = (\mathbf{d} - \mathbf{M}(\mathbf{p}))^t (\mathbf{d} - \mathbf{M}(\mathbf{p})) \tag{8}$$

The regularization function describes the squared differences between the regularization values $\mathbf{M}(\mathbf{p})$ and the initial regularization observations d derived from the assignment of facies-specific K-values to each pilot point.

Pilot points are employed in great numbers to delineate the identified structures. In most cases, the number of pilot points necessary to maintain the basic structure from the tomogram will be in the order hundreds, and the calibration procedure accordingly will be computationally demanding. As a remedy, application of

parallelization and subspace regularization is suggested by Doherty [65]. The goal of subspace regularization is to decrease the number of pilot points during the inversion, in order to reduce the computational time. The underlying principle is the same as that for the null-space energy maps introduced above for travel-time inversion (Eqs. (2) and (3)). To get insights in the singular values matrix, the condition number (ratio of the largest singular value to the smallest singular value) can be scrutinized. The condition number qualifies the linear dependency of the equations representing the tomographic system. Note, for each unknown (i.e. each pilot point) one equation has to be solved. A large condition number indicates that some equations of the system can be expressed as linear combination of the others. Thus it is possible to reduce the number of equations or pilot points, respectively, after each iteration step. For example, in this study we could reduce the number of pilot points from 373 to 233. In doing so, the resulting inversion time could substantially be reduced.

3. Study site and experimental set-up

3.1. Herten aquifer analogue

For the demonstration of the sequential HT inversion procedure, we selected a "known reality": a high-resolution 3D aquifer analogue serves as study site. Instead of practical testing, computer-based experiments will be conducted. The analogue offers us the opportunity to work with realistic, complex and multiscale heterogeneities, and in contrast to field investigation at similar sites, the subsurface structures are known. This will facilitate a straightforward validation by comparison with the inversion results.

The aguifer analogue data was collected in SW Germany in the town of Herten, close to the Rhine river at the Swiss border [67]. A gravel pit in excavation offered direct insight into the decimeterscale sedimentary facies distribution of the unconsolidated gravel, which was formed about ten thousand years ago as fluvio-glacial sediment during the retreat of the Rhine glacier. During excavation, the structures found in six parallel vertical cross-sections (7 m height, 16 m with, 2 m distance) were recorded taking field samples, photographs and drawings. Based on lab measurements of porosity and hydraulic conductivity, hydrofacies mosaics that delineate sedimentary horizontal layers overlaying cross-beddings with significant small-scale conductivity contrasts were obtained. The cross-sections were interpolated by Maji and Sudicky [68] and utilized in the HT application by Hu et al. [40]. The more recent multiple points based interpolation by Comunian et al. [69] better preserves 3D continuity of the sedimentary units and thus is favored for our study. One specific 3D analogue realization (Fig. 3) is selected to simulate a highly heterogeneous aquifer, with the conductivity values of 10 hydro(geological) facies ranging from 6×10^{-7} to 1×10^{-1} m/s.

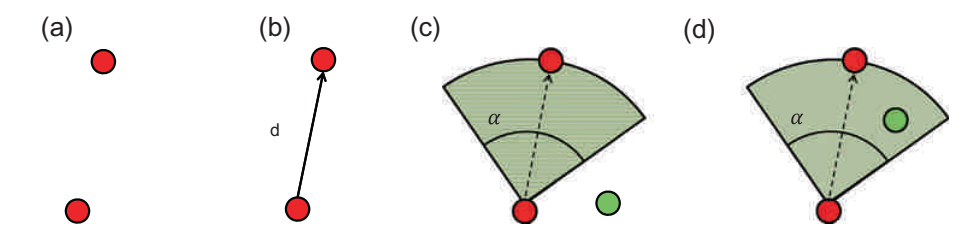


Fig. 2. Adjacency conditions based on a 2-D slice of the three-dimensional domain. (a) Both red pilot points pertain to the same cluster category. (b) The distance, *d*, between the pilot points is smaller than the average length of the cluster in horizontal direction, *r*. In the situation depicted in (c) no pilot point from a different cluster (pilot point displayed in green color) is within the zone of influence and therefore the pilot points will be connected. In (d) the requirement is not met, a pilot point from a different cluster (pilot point displayed in green color) is within the zone of influence, and hence, the two pilot points will be not connected. (For interpretation of the references to color in this figure legend, the reader is referred to the web version of this article.)

3.2. Numerical simulation and configuration of cross-well test

The analogue is implemented in the center of a numerical groundwater flow model, embedded in a homogeneous hull ($\Delta x = 600 \text{ m}$; $\Delta y = 116 \text{ m}$; $\Delta z = 7 \text{ m}$) to minimize boundary effects. In the heterogeneous core model, the numerical mesh is composed of about six millions uniform tetrahedrons, with telescopic lateral coarsening in the homogeneous surrounding. Constant head boundary conditions are imposed at the two faces (perpendicular to the longitudinal axes) of the homogeneous hull. The rest of the faces have no flow boundary condition. The hydraulic properties of the heterogeneous core corresponds to a selected realization of the Herten aquifer analogue, and the hull is specified the analogue's median values. More information about the design of the groundwater flow model is provided as Supplementary Information.

4. Results and discussion

4.1. Experiment – pressure response

The hydraulic cross-well simulations were performed with Comsol Multiphysics. In Fig. 3 the spatial position of the test and the six observation wells, within the aquifer analogue environment, are displayed. The distance between the test and the observation wells is always 3.5 m. The test well is subdivided into six vertical sectors that represent the screened intervals. In each screened interval of the test well a hydraulic test was simulated and the transient pressure response was recorded in each observation well in six different depths. Hence, the derived data base

consists of 216 ($6 \times 6 \times 6$) pressure response curves. In this model, the screened intervals of the test well were implemented implicitly as 1D-elements with a length of 0.5 m. The pressure response curves were recorded directly at the respective nodes.

4.2. Diffusivity tomograms

Six vertical sections a-f, are obtained by diffusivity reconstruction between source and receivers. For this, all source-receiver combinations with an angle of 40° and less between the center of the packer and observation point are taken. This threshold is set to capture the mainly horizontal and sub-horizontal structures, while eliminating those responses which are more vertical and thus, potentially across the main structures [40]. The first derivative of the head response data is used to determine the peak time and the used travel-time diagnostic t - 10%. The eikonal solver CAT3D translates this for a given regular grid in a diffusivity tomogram. As initial model domain, a relatively coarse grid of 10×12 cells is chosen, because the applied inversion scheme includes no regularization terms. To increase the nominal resolution of the coarse grid, we utilized the staggered grid method developed by Vesnaver and Böhm [70] and applied in the context of hydraulic tomography by Brauchler et al. [71]. The method is based on the displacement of the initial grid in all directions. The displacement rates in the Δx and Δy are 0.15 and 0.16 m of the cell length in both directions, respectively. For each grid position, we performed an inversion and received a slightly different image. In total we performed 16 single inversions and determined the arithmetic mean of all grids by staggering them. The diffusivity tomograms

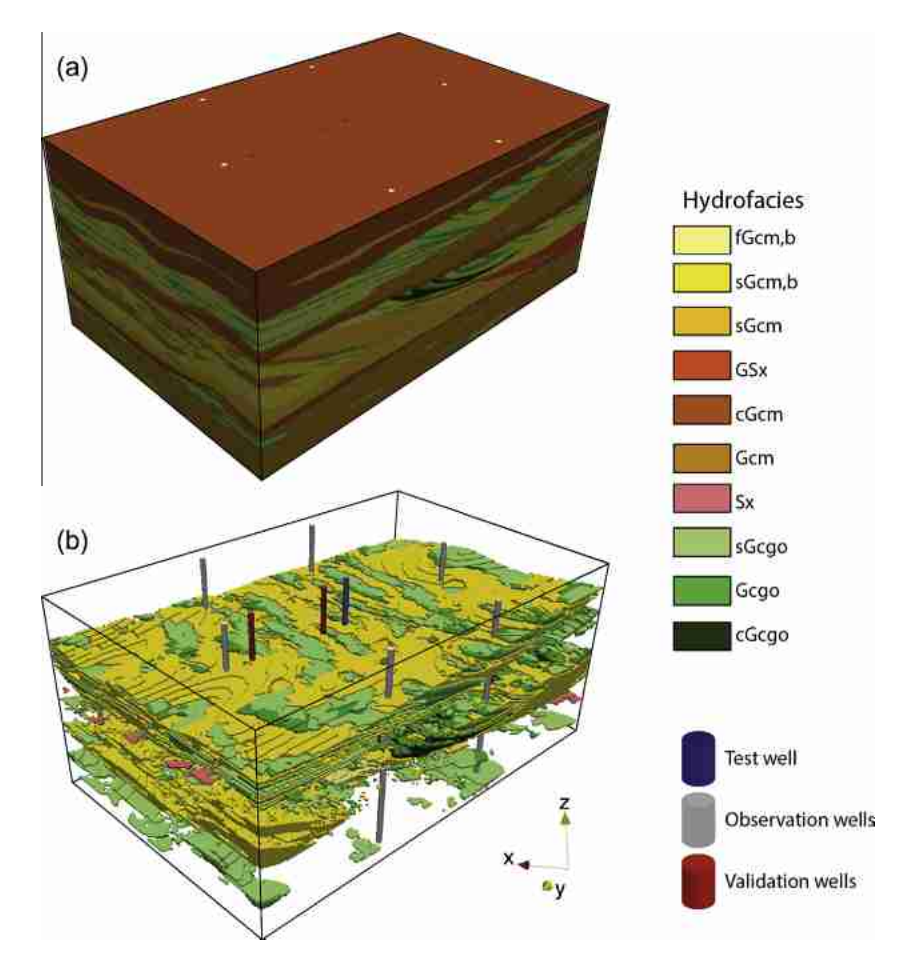


Fig. 3. Realization of Herten aquifer analogue used as application case; (a) hydrofacies (b) only high conductivity facies and borehole locations (blue: source well, grey: observation wells, red: validation wells). (For interpretation of the references to color in this figure legend, the reader is referred to the web version of this article.)

displayed in Fig. 4 is composed of 40 cells in *x*- and 48 cells in *y*-direction. Note that each of the six vertical sections was inverted separately, in two-dimensions, applying the technique described above.

The original diffusivity distributions of the six 5 m \times 6 m crosssections a-f are shown in the first column of Fig. 4. For the calculation of the diffusivity distribution we assumed a homogeneous specific storage distribution and utilized the relationship $D = K/S_s$. All share a central mostly elongated zone with local high diffusivity values of up to 1400 m²/s. This stems from coarse open framework gravel deposits that dominate the central alternating sequence in the aquifer analogue. This sequence is differentiated as m-scale architectural element in Bayer et al. [67]. Cross-beddings are visible here, and also in the other, similar high-diffusivity part at vertical position z = 4.5-5.5 m. When comparing all cross-sections, orientation of cross-beddings and inclination of layers apparently depends on the orientation of the section, but generally sub-horizontal structures are found. There is one dominant architectural element, which appears most uniform and persistent: the gravel sheet deposits on top, bottom and between the alternating sequences, which are visualized by homogeneous zones of light blue.

The results from travel-time inversion, the *D*-tomograms, are depicted in the second column of Fig. 4. We chose a different color scale for the true and reconstructed diffusivity distribution in order to highlight the structural information contained in the diffusivity tomograms. The first impression is that the main structures are somewhat reproduced but not perfectly localized and with limited resolution. The resolution of travel-time inversion is constrained by the number of source-receiver combinations that are evaluated, and thus in our application the dm-(sub)scale heterogeneities of the analogue can hardly be reconstructed. However, the m-scale structures, which originate from the main architectural elements found in the aquifer analogue, are well identified in most crosssections. Tomogram "a", for example, properly reproduces position and form of the high-diffusivity zones, even if diffusivity at the section bottom is overestimated. In the other sections, the two alternating sequences are identified as separate (b, c, f) or a merged zone (d. e). An evident example is the upper area of section "e". where high-diffusivity values (orange and red) are mixed with low diffusivity values (cerulean), limiting the reconstruction capacity of this inversion step. Least consistent are the bottom and the lateral boundaries of the tomograms, and even if the original structure is reproduced, absolute diffusivity values are often far from the "real" information given by the analogue. This motivates to extract mainly the structural information rather than absolute diffusivity estimates from the travel-time inversion results.

In order to assess the spatial reliability of the *D*-tomograms, null space energy maps are produced (Fig. 5). Two major fields can be distinguished. In the outer part of the model, where no trajectory is passing through, null space energy values are close to one (i.e. low reliability). In the rest of the domain we find intermediate values. There are also fields of low reliability in this inner domain, which are characterized by low diffusivity values. This reflects that trajectories try to avoid such zones, and this decreases the trajectory density. A good example can be observed in section "f" (Fig. 5) where a low reliability zone is present in vertical position 1–2 m, corresponding to small diffusivity values ranging from 27 to 35 m²/s (Fig. 4). As a conclusion, the null-space maps are plausible, and they offer valuable insight into the reliability of the *D*-tomograms. In particular, they provide reasons for the badly characterized fringe in most cross-sections.

4.3. Conceptual maps

The next step towards characterizing the structures is the cluster analysis. The aim of cluster analysis is to approximate – on a

resolution constrained by the tomogram accuracy – the hydro(geological) facies distribution that controls flow in the aquifer.

The cluster analysis is applied for all those diffusivity values that are associated with low null space energy, that is, below 0.97. Hence, the diffusivity values of the outer part of the model domain and zones characterized by low diffusivity values, both associated with low reliability, are excluded. To apply k-means cluster analysis, a suitable number of clusters must be defined. Therefore, we utilized hierarchical clustering. The dendrogram plot, displayed in Fig. 6, shows that the maximum distance between the two most separated diffusivity values is 14. If we assign all diffusivity values to two clusters, the maximum distance between the two most separated diffusivity values within the two clusters is only six. This indicates that the diffusivity distributions are dominated by two groups. Thus, two clusters will be used to group the diffusivity values in two hydrofacies. In order to simplify the dendrogram plot, the first two hierarchies are not displayed in Fig. 6. The resulting structural maps are presented in the third column of Fig. 4. Where no information is available due the low reliability of some points, adjacent values are interpolated using ordinary kriging. This results in the smoothing of the structures and loss of some details suggested by travel-time inversion, such as can be seen for example in the upper half of section "c".

4.4. Hydraulic conductivity reconstruction

The calibration step estimates K-values in 3-D, while preserving the structures identified during travel-time inversion (Eq. (6)). For the latter, the mission is to locate the pilot points where they are able to reproduce the original hydrofacies distribution that is approximated by the clusters. For the application case, the goal is to heavily constrain the structure, and accordingly a set of 280 pilot points is assigned, based on the six conceptual maps (Fig. 4, third column). The 2-D section-based HT method is not capable of interpreting the space in between the six examined source-receiver combinations. In order to facilitate 3-D parameter estimation, six auxiliary vertical sections are introduced (Fig. 7), with a regular grid of 16 pilot points each. Ordinary kriging is applied as spatial interpolator (e.g. [61]) between the pilot points after each iteration step in order to determine the hydraulic conductivity values between them. Each pilot point contains the necessary information, that is, spatial coordinates and cluster category, for the smoothing Tikhonov regularization. As an essential element of regularization, the adjacency matrix states if two pilot points are contiguous or not. It is computed after inspecting the conceptual maps to specify suitable parameter ranges for r and α . Spatial analysis on all maps yields a mean length of r = 4.5 m. The average angle is $\alpha = 42^{\circ}$. The pilot points are connected by 14,032 edges. Fig. 8 shows the pilot points of section "a", connected by 1565 edges.

For the pilot-point based inversion, parallelized implementation and cloud computing was utilized [72,73]. This was realized with a heterogeneous hardware configuration with a PC (i7 3.4 GHz, 16 Gb RAM), two work stations (8x Xeon 3.33 GHz, 24 Gb RAM and 32x Xeon 3.1 GHz, 64 Gb RAM) and two virtual instances in a cloud (Amazon EC2 m1.xlarge (http://aws.amazon.com/ec2), see [73]). By parallelization, the computing time for the entire sequential inversion procedure was reduced from almost 300 h on a single personal computer to 40 h, whereby one single forward model run took 10 min. The calculation time for the travel time inversion was approximately 20 s for one profile on a single personal computer and hence, computing time for the travel-time inversion can be considered negligible in comparison to the pilot-point based inversion step.

In Fig. 4, the agreement between the conceptual maps based on the structures anticipated by diffusivity clustering and the final reconstructed *K*-distribution is still visible, although the initial

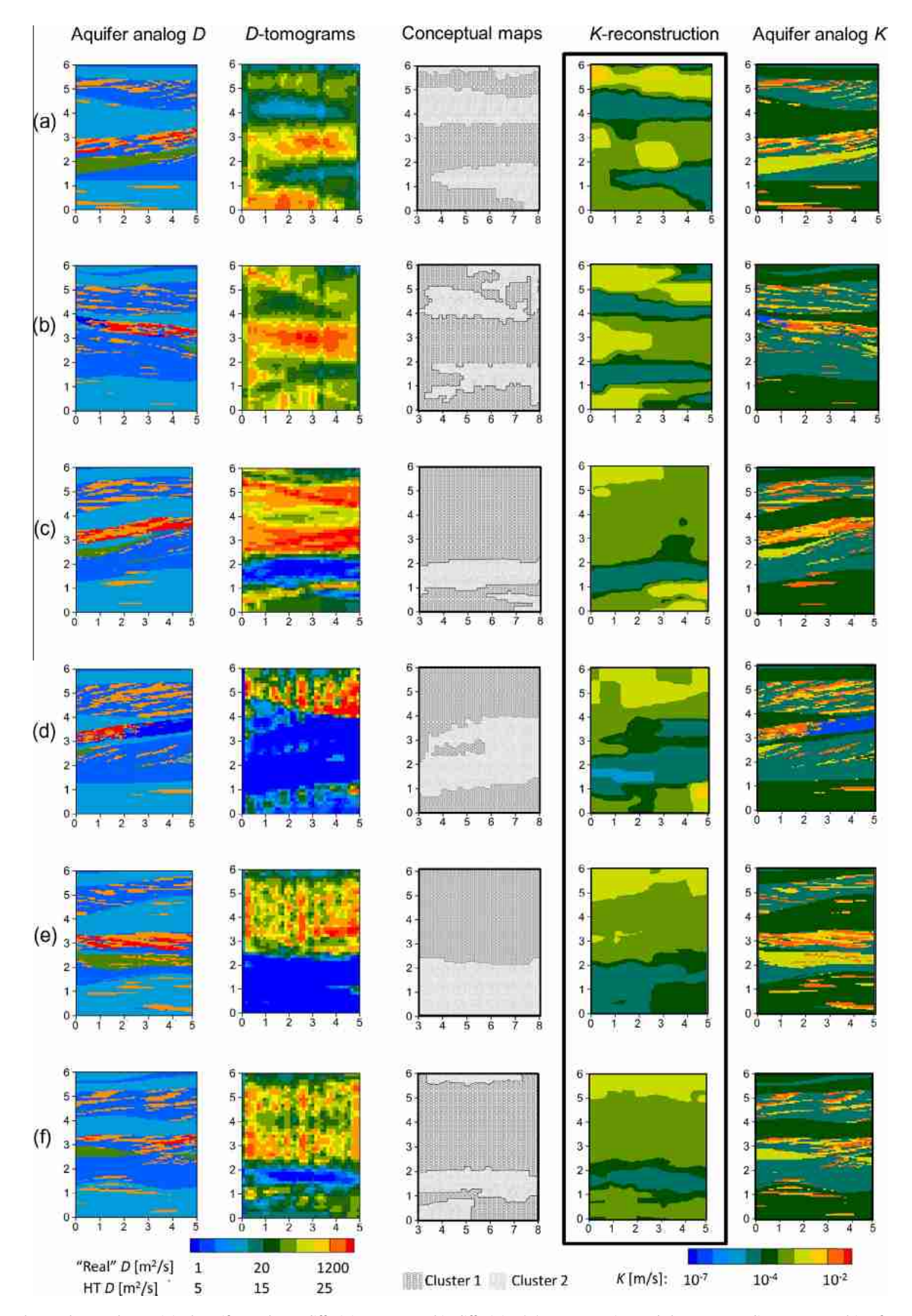


Fig. 4. First three columns show original aquifer analogue diffusivity, tomographic diffusivity (*D*) reconstruction and the corresponding zones resulting from the cluster analysis. Final reconstructed hydraulic conductivity distribution is shown in 4th column, and for comparison the true hydraulic conductivity distribution of the aquifer analogue is shown in column five.

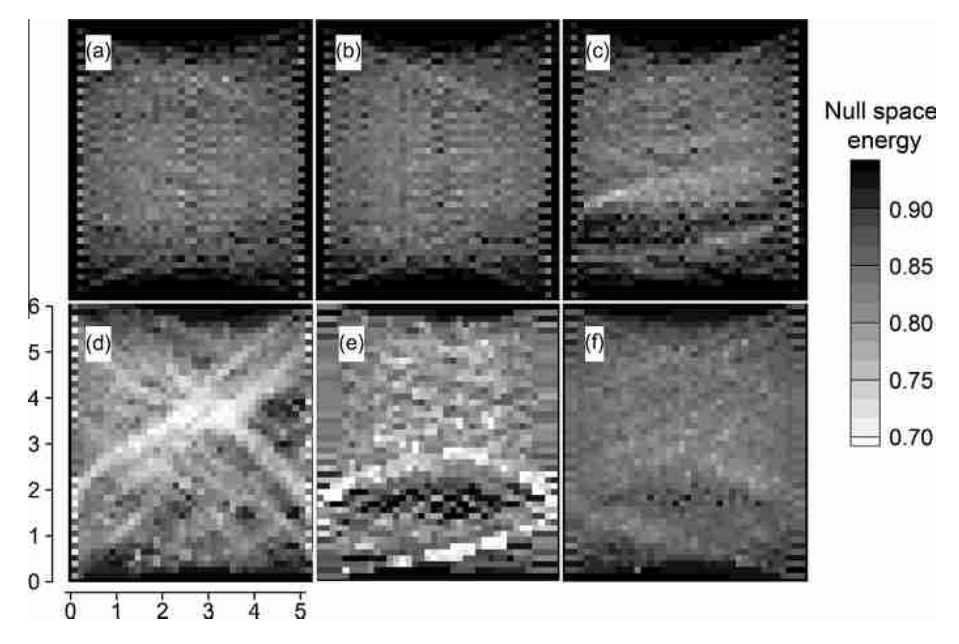


Fig. 5. Null space energy maps of the corresponding diffusivity tomograms a-f shown in Fig. 4 (scale in meters).

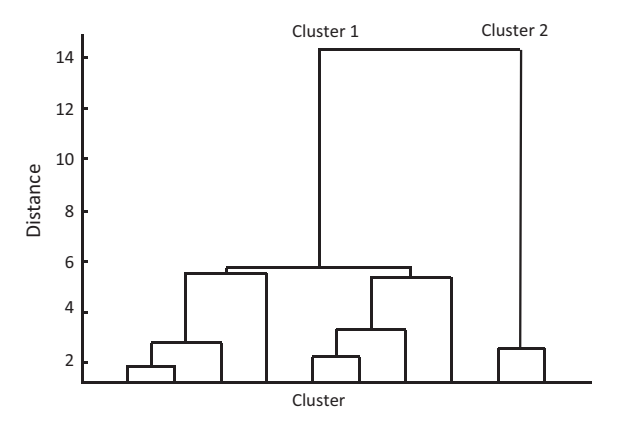


Fig. 6. Dendrogram based on the diffusivity values derived from the travel time inversion.

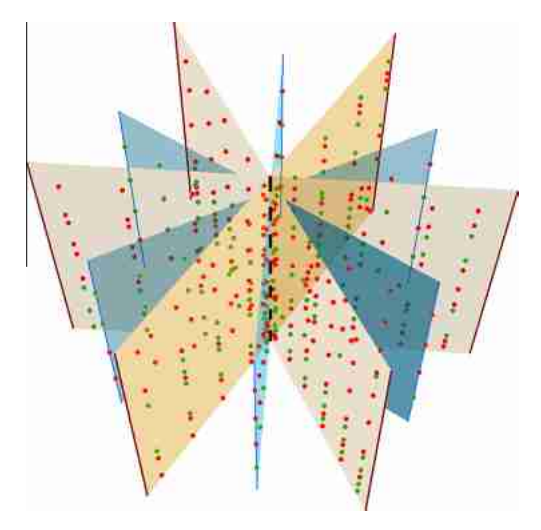


Fig. 7. Illustration of pilot point distributions, the source-receiver cross-sections (orange) and auxiliary sections (blue). (For interpretation of the references to color in this figure legend, the reader is referred to the web version of this article.)

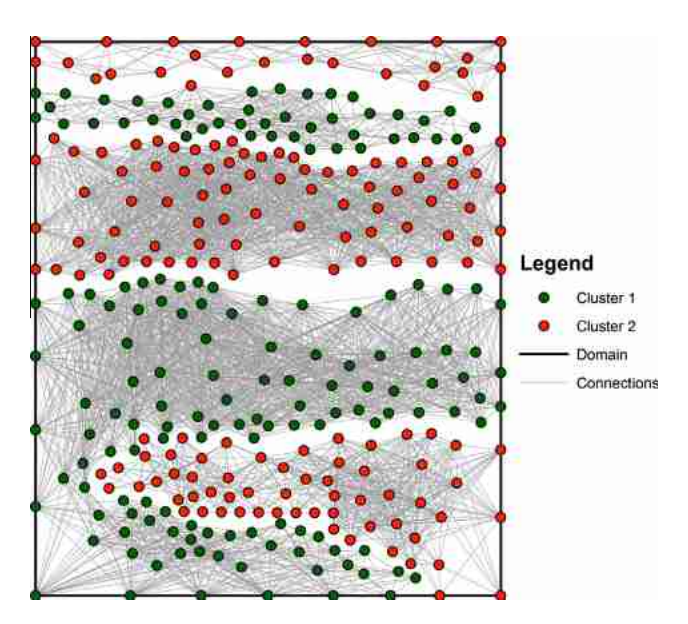


Fig. 8. Graph representing the pilot points relationships in section a.

K-field was adjusted in order to fit the observed transient pressure data. The final *K*-fields obtained from the inversion are compared to the original aquifer analogue *K* distribution in the fifth column of Fig. 4. At first sight, the reconstructed sections are at much coarser scale than the original ones. The limited resolution of the HT based inversion, however, is expected in view of the experimental set-up. With a screen interval length of half a meter the original dm-scale heterogeneity can hardly be extracted from the recorded pressure-responses.

In all sections, we can see that layers of high and low conductivity in the same order of magnitude are nicely reproduced. There are some examples, where the inversion results could be improved. For example, the upper alternating sequence (about $y=5\,$ m), with high and low K cross-beddings, is not well identified in most sections and not precisely localized in sections "a" and "b". This may reflect that even if high conductivity facies are present here, the

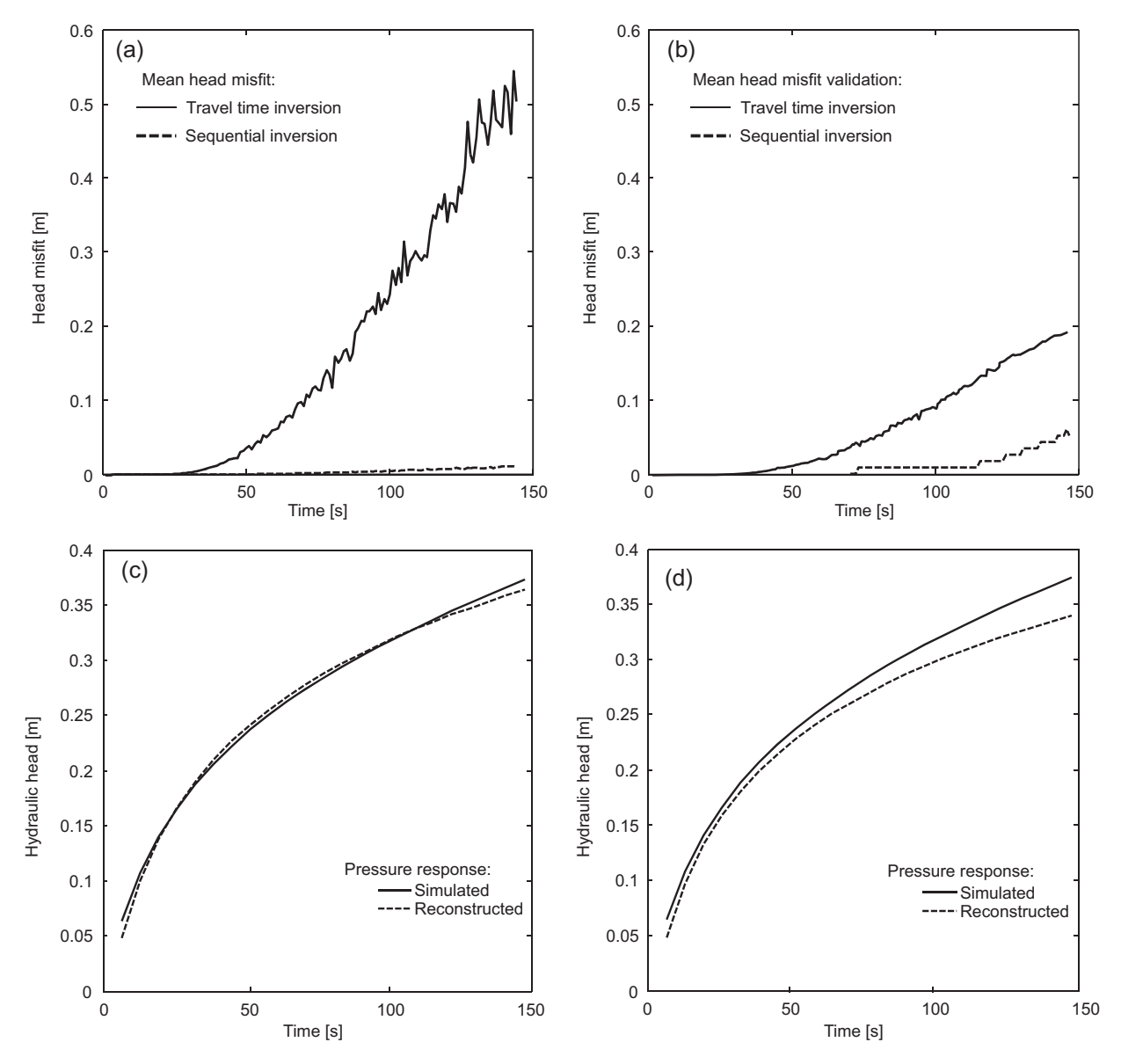


Fig. 9. Mean head misfit for travel time and sequential inversions and comparison of the simulated and the reconstructed pressure response curves not used for the inversion: (a) misfit computed with pressure response curves used in inversion, (b) misfit computed with pressure response curves used only for validation purposes, (c) best fit of the simulated pressure response curves, (d) worst fit of the simulated pressure response curves.

connectivity is not sufficient to have a substantial hydraulic effect on the m-scale. In contrast, the low conductivity area at about y = 2 m is an excellent example for successful reconstruction. This is especially the case in sections b, c, d, and f.

Additional to the visual assessment of the results, validation with a series of modeled pumping tests is carried out. This is done by 18 pressure response curves that were not used for the HT inversion, whereby the spatial position of the test and the observation well is displayed in Fig 3. Three tests were simulated in a depth of 1.7, 3.4, and 5.1 m and the pressure response curves of each test were recorded in six different depths (1, 2, 3, 4, 5, 6 m) for 145 s. For the validation, the time dependent mean misfit between the heads simulated with the original analogue and the reconstructed block is shown in Fig. 9b. This is complemented with Fig. 9a, which depicts the same results but for the head responses applied in the calibration. Both figures clearly show very small misfits, which slightly increase with simulation time to about 0.05 m. Non-used head responses are slightly worse than those utilized in the calibration. Note, the misfits are displayed in absolute values. For this reason the misfits are increasing if the pressure head is increasing in the observation well. The figures also display the much more significant discrepancies when only employing travel-time inversion. The respective *K*-distributions are derived from the *D*-tomograms assuming we know the true specific storage field. The mean misfit is more than one order of magnitude higher, and this substantiates the need for an additional adjustment of the spatial *K*-distribution. For a better comparison of the simulated and the reconstructed pressure response curves, we displayed exemplarily the best and the worst fit in Fig. 9c and d. More details can be found as Supplementary Information, where we provide the comparison of all 18 simulated and reconstructed pressure response curves.

5. Conclusions

The presented inversion procedure for HT extracts structural information on aquifer heterogeneity from diffusivity tomograms, and integrates this to constrain pilot-point based three-dimensional hydraulic conductivity estimation. This tackles the deficits of separately existing methods by their symbiotic combination.

Travel-time inversion facilitates a fast reconstruction of a cross-section between two wells, based on multiple head stimulations and responses between the wells that act as source and receiver. However, only the diffusivity D = K/S is obtained, and this is not sufficient to derive the hydraulic conductivity, K, distribution. Existing methodologies [1,40], for example, propose statistical clustering and zonal calibration, but this means that the "soft information" from the diffusivity tomograms are taken as hard data with a crucial bias introduced by the type of clustering method used. Ideally, structural insight obtained from HT is exploited as much as possible, but not more than necessary and this insight constrains the subsequent calibration of the K-field.

With this perspective, the diffusivity tomogram here is adopted as initial guess of the K-field structure. Utilizing the null space energy maps we are able to judge the reliability of the tomograms. In fact, these maps could be used to guide additional experiments, in order to arrive at tomograms of high reliability at all locations of interest. This is of particular interest in the context of data worth based optimal field investigation (e.g. [74]). The null-space maps also support reliable clustering, and this is where they are applied in our procedure. Clustering, however, is not employed to determine a fixed zonation, rather than to instruct how to position pilot points. This way, the structural information from tomographic testing is nicely conveyed as soft information to the K-field calibration. Missing a priori knowledge to constrain pilot- point inversion is often a major shortcoming, when this method is used for calibration. This also applies to the regularization step to interpolate between the points. By establishing adjacency conditions of pilot points in a graph theoretical framework, a new step is included to guide the regularization. As a result, a sequential procedure is developed that follows two objectives: Keeping identified structures and finding a possible K-distribution. Structures, however, are not implemented as fixed zones. Instead, regularization-based inversion facilitates a flexible spatial adjustment. A worthwhile topic for future research would be to utilize the further development of the eikonal-based inversion approach proposed by Brauchler et al. [71]. The approach allows for the inversion of pumping test signals and to reconstruct the diffusivity, as well as the storativity field using calculation efficient ray tracing techniques. By utilizing the information content of the diffusivity, as well as the reconstructed storativity tomogram, the proposed pilot-point based inversion scheme could be further developed with respect to reconstruct the spatial storativity distribution.

As an example, a highly heterogeneous aquifer analogue is selected, which is implemented in a groundwater model. The analogue of the Herten case study is very realistic, and exhibits strong conductivity contrasts on the decimeter scale. It represents a challenge for HT as any other related field experiments. It is clear that the used twelve well screens can hardly capture this smallscale variability, and this is illustrated by the resolution of the inverted six cross-sections. Within the resolution capability, however, coarse scale structures are reproduced. What is more, the three-dimensional analogue could be reconstructed and the validation with pumping tests succeeded. Still, the presented reconstruction represents only one of many possible realizations of the spatial K-distribution. Even if the combined use of different data and methods constrains K-field calibration, the inversion problem is still ill posed. Thus, further work will concentrate on including more data, which is additional structural information, such as geological expertise, or stems from additional measurement, such as near surface geophysics or tracer testing.

Acknowledgments

The investigations were conducted with the financial support of the Swiss National Science Foundation to the projects "A field assessment of high-resolution aquifer characterization: An integrated approach combining hydraulic tomography and tracer tomography" under grant number 200021_140450 / 1, and the CCES funded project "RECORD Catchment". Finally, we thank Michael Cardiff and the four other anonymous reviewers for their helpful comments and suggestions that improved the quality of the manuscript.

Appendix A. Supplementary data

Supplementary data associated with this article can be found, in the online version, at http://dx.doi.org/10.1016/j.advwatres.2013. 10.002.

References

- Brauchler R, Hu R, Dietrich P, Sauter M. A field assessment of high-resolution aquifer characterization based on hydraulic travel time and hydraulic attenuation tomography. Water Resour Res 2011;47:W03503. http://dx.doi.org/10.1029/2010WR009635.
- [2] Berg SJ, Illman WA. Capturing aquifer heterogeneity: comparison of approaches through controlled sandbox experiments. Water Resour Res 2011;47:W09514. http://dx.doi.org/10.1029/2011wr010429.
- [3] Illman WA, Zhu J, Craig AJ, Yin D. Comparison of aquifer characterization approaches through steady state groundwater model validation: a controlled laboratory sandbox study. Water Resour Res 2010;46. http://dx.doi.org/10.1029/2009wr007745.
- [4] Illman WA, Berg SJ, Alexander M. Cost comparisons of aquifer heterogeneity characterization methods. Ground Water Monit Rem 2012;32:57–65. http://dx.doi.org/10.1111/i.1745-6592.2011.01376.x.
- [5] Mersereau R, Oppenheim AV. Digital reconstruction of multi-dimensional signals from their projections. IEEE Proc 1974;62:1319–38. ISSN: 0018-9219.
- [6] Bohling GC. Hydraulic tomography in two-dimensional, steady-state groundwater flow. Eos Trans AGU 1993;74(16). (Spring Meet Suppl, 141). http://dx.doi.org/10.1007/978-3-540-75384-1_6.
- [7] Tosaka H, Masumoto K, Kojima K. Hydropulse tomography for identifying 3-D permeability distribution. In: High level radioactive waste management, conference proceeding paper; 1993.
- [8] Gottlieb J, Dietrich P. Identification of the permeability distribution in soil by hydraulic tomography. Inverse Prob 1995;11:353–60. http://dx.doi.org/10.1088/0266-5611/11/2/005
- [9] Yeh T-CJ, Liu S. Hydraulic tomography: development of a new aquifer test method. Water Resour Res 2000;36:2095–105. http://dx.doi.org/10.1029/2000WR900114.
- [10] Brauchler R, Liedl R, Dietrich P. A travel time based hydraulic tomographic approach. Water Resour Res 2003;39:1370. http://dx.doi.org/10.1029/2003WR002262.
- [11] Zhu J, Yeh T-CJ. Characterization of aquifer heterogeneity using transient hydraulic tomography. Water Resour Res 2005;41:W07028. http://dx.doi.org/10.1029/2004WR003790.
- [12] Xiang J, Yeh T-CJ, Lee C-H, Hsu K-C, Wen J-C. A simultaneous successive linear estimator and a guide for hydraulic tomography analysis. Water Resour Res 2009;45:W02432. http://dx.doi.org/10.1029/2008WR007180.
- [13] Liu S, Yeh T-CJ, Gardiner R. Effectiveness of hydraulic tomography: sandbox experiments. Water Resour Res 2002;38:1034. http://dx.doi.org/10.1029/20214thpe02032
- [14] Liu X, Illman WA, Craig AJ, Zhu J, Yeh T-CJ. Laboratory sandbox validation of transient hydraulic tomography. Water Resour Res 2007;43:W05404. http://dx.doi.org/10.1029/2006WR005144.
- [15] Illman WA, Craig AJ, Liu X. Practical issues in imaging hydraulic conductivity through hydraulic tomography. Ground Water 2008;46(1):120–32. http://dx.doi.org/10.1111/ji.1745-6584.2007.00374.x.
- [16] Illman WA, Liu X, Craig A. Steady-state hydraulic tomography in a laboratory aquifer with deterministic heterogeneity: multi-method and multiscale validation of hydraulic conductivity tomograms. J Hydrol 2007;341:222–34. http://dx.doi.org/10.1016/j.jhydrol.2007.05.011.
- [17] Yin D, Illman WA. Hydraulic tomography using temporal moments of drawdown recovery data: a laboratory sandbox study. Water Resour Res 2009;45:W01502. http://dx.doi.org/10.1029/2007WR006623.
- [18] Illman WA, Berg SJ, Liu X, Massi A. Hydraulic/partitioning tracer tomography for DNAPL source zone characterization: small-scale sandbox experiments. Environ Sci Technol 2010;44:8609–14. http://dx.doi.org/10.1021/es101654j.
- [19] Bohling GC, Butler Jr JJ, Zhan X, Knoll MD. A field assessment of the value of steady shape hydraulic tomography for characterization of aquifer heterogeneities. Water Resour Res 2007;43:W05430. https://dx.doi.org/10.1029/2006WR004932.
- [20] Bohling GC. Sensitivity and resolution of tomographic pumping tests in an alluvial aquifer. Water Resour Res 2009;45:W02420. http://dx.doi.org/10.1029/2008WR007249.
- [21] Berg SJ, Illman WA. Three-dimensional transient hydraulic tomography in a highly heterogeneous glaciofluvial aquifer-aquitard system. Water Resour Res 2011;47:W10507. http://dx.doi.org/10.1029/2011wr010616.

- [22] McDermott CI, Sauter M, Liedl R. New experimental techniques for pneumatic tomographical determination of the flow and transport parameters of highly fractured porous rock samples. J Hydrol 2003;278:51–63. http://dx.doi.org/ 10.1016/S0022-1694(03)00132-X.
- [23] Illman WA, Liu X, Takeuchi S, Yeh T-CJ, Ando K, Saegusa H. Hydraulic tomography in fractured granite: Mizunami underground research site, Japan. Water Resour Res 2009;45:W01406. http://dx.doi.org/10.1029/2007WR006715.
- [24] Sharmeen R, Illman WA, Berg SJ, Yeh T-CJ, Park Y-J, Sudicky EA, et al. Transient hydraulic tomography in a fractured dolostone: laboratory rock block experiments. Water Resour Res 2012;48:W10532. http://dx.doi.org/10.1029/2012wr012216.
- [25] Bohling GC, Butler JJ. Inherent limitations of hydraulic tomography. Ground Water 2010;48:809–24. http://dx.doi.org/10.1111/ji.1745-6584.2010.00757.x.
- [26] Cardiff M, Bharrash W. 3-D transient hydraulic tomography in unconfined aquifers with fast drainage response. Water Resour Res 2011;47:W12518. http://dx.doi.org/10.1029/2010wr010367.
- [27] Lavenue M, de Marsily G. Three-dimensional interference test interpretation in a fractured aquifer using the pilot point inverse method. Water Resour Res 2001;37:2659–75. http://dx.doi.org/10.1029/2000WR000289.
- [28] Vesselinov VV, Neuman SP, Illman WA. Three-dimensional numerical inversion of pneumatic cross-hole tests in unsaturated fractured tuff: 1. Methodology and borehole effects. Water Resour Res 2001;37:3001–17. http://dx.doi.org/10.1029/2000wr000133.
- [29] Vesselinov VV, Neuman SP, Illman WA. Three-dimensional numerical inversion of pneumatic cross-hole tests in unsaturated fractured tuff: 2. Equivalent parameters, high-resolution stochastic imaging and scale effects. Water Resour Res 2001;37:3019–41. http://dx.doi.org/10.1029/2000wr000135.
- [30] Castagna M, Becker MW, Bellin A. Joint estimation of transmissivity and storativity in a bedrock fracture. Water Resour Res 2011;47:W09504. http://dx.doi.org/10.1029/2010wr009262.
- [31] Castagna M, Bellin A. A Bayesian approach for inversion of hydraulic tomographic data. Water Resour Res 2009;45:W04410. http://dx.doi.org/10.1029/2008wr007078.
- [32] Li W, Englert A, Cirpka OA, Vereecken H. Three-dimensional geostatistical inversion of flowmeter and pumping test data. Ground Water 2008;46:193-201. http://dx.doi.org/10.1111/j.1745-6584.2007.00419.x.
- [33] Straface S, Yeh TCJ, Zhu J, Troisi S, Lee CH. Sequential aquifer tests at a well field, Montalto Uffugo Scalo, Italy. Water Resour Res 2007;43:W07432. http://dx.doi.org/10.1029/2006wr005287.
- [34] Bohling GC, Butler Jr JJ, Zhan X, Knoll MD. A field assessment of the value of steady shape hydraulic tomography for characterization of aquifer heterogeneities. Water Resour Res 2007;43:W05430. http://dx.doi.org/10.1029/2006wr004932.
- [35] Cardiff M, Kitanidis PK. Bayesian inversion for facies detection: an extensible level set framework. Water Resour Res 2009;45:W10416. http://dx.doi.org/10.1029/2008wr007675.
- [36] Berg SJ, Illman WA. Improved predictions of saturated and unsaturated zone drawdowns in a heterogeneous unconfined aquifer via transient hydraulic tomography: laboratory sandbox experiments. J Hydrol 2012;470:172–83. http://dx.doi.org/10.1016/i.ihvdrol.2012.08.044.
- [37] Brauchler R, Hu R, Vogt T, Al-Halbouni D, Heinrichs T, Ptak T, et al. Cross-well slug interference tests: an effective characterization method for resolving aquifer heterogeneity. J Hydrol 2010;384:33–45. http://dx.doi.org/10.1016/j.iihydrol.2010.01.004.
- [38] Brauchler R, Doetsch J, Dietrich P, Sauter M. Derivation of site-specific relationships between hydraulic parameters and p-wave velocities based on hydraulic and seismic tomography. Water Resour Res 2012;48:W03531. http://dx.doi.org/10.1029/2011wr010868.
- [39] Vasco DW, Keers H, Karasaki K. Estimation of reservoir properties using transient pressure data: an asymptotic approach. Water Resour Res 2000;36:3447–65. http://dx.doi.org/10.1029/2000wr900179.
- [40] Hu R, Brauchler R, Herold M, Bayer P. Hydraulic tomography analog outcrop study: combining travel time and steady shape inversion. J Hydrol 2011;409:350-62, http://dx.doi.org/10.1016/j.jhydrol.2011.08.031.
- 2011;409:350-62. http://dx.doi.org/10.1016/j.jhydrol.2011.08.031.
 [41] Dietrich P, Leven C. Direct push-technologies. In: Kirsch R, editor. Groundwater geophysics. Berlin Heidelberg: Springer; 2006. p. 321-40. http://dx.doi.org/10.1007/3-540-29387-6. 11.
- [42] Cardiff M, Barrash W, Kitanidis PK. A field proof-of-concept of aquifer imaging using 3-D transient hydraulic tomography with modular, temporarilyemplaced equipment. Water Resour Res 2012;48:W05531. http://dx.doi.org/10.1029/2011wr011704.
- [43] Brauchler R, Cheng J-T, Dietrich P, Everett M, Johnson B, Liedl R, et al. An inversion strategy for hydraulic tomography: coupling travel time and amplitude inversion. J Hydrol 2007;345:184–98. http://dx.doi.org/10.1016/i.jihydrol.2007.08.011.
- [44] Brauchler R, Böhm G, Leven C, Dietrich P, Sauter M. A laboratory study of tracer tomography. Hydrogeol J 2013;21:1–10. http://dx.doi.org/10.1007/s10040-013-1006-z.
- [45] Böhm G, Aldo V. Relying on a grid. J Seismic Explor 1996;5:169-84.
- [46] MacQueen J. Some methods for classification and analysis of multivariate observations. In: Proceedings of the fifth Berkeley symposium on mathematical statistics and probability. California, USA; 1967. p. 14.
- [47] Anderberg MR. Cluster analysis for applications. DTIC Document; 1973.

- [48] Hartigan JA. Clustering algorithms. John Wiley & Sons Inc.; 1975. ISBN: 047135645X.
- [49] Sun R, Yeh T-CJ, Mao D, Jin M, Lu W, Hao Y. A temporal sampling strategy for transient hydraulic tomography analysis. Water Resour Res 2012:3881–96. http://dx.doi.org/10.1002/wrcr.20337.
- [50] Wu C-M, Yeh T-CJ, Zhu J, Lee TH, Hsu N-S, Chen C-H, et al. Traditional analysis of aquifer tests: comparing apples to oranges? Water Resour Res 2005;41:W09402. http://dx.doi.org/10.1029/2004wr003717.
- [51] de Marsily G, Lavendan C, Boucher M, Fasanino G. Interpretation of interference tests in a well field using geostatistical techniques to fit the permeability distribution in a reservoir model. In: Verly G, David M, Journel AG, Marechal A, editors. Geostatistics for natural resources characterization, NATO ASI, Ser C, vol. 182; 1984. p. 831–49.
- [52] Certes C, de Marsily G. Application of the pilot point method to the identification of aquifer transmissivities. Adv Water Resour 1991;14:284–300. http://dx.doi.org/10.1016/0309-1708(91)90040-U.
- [53] RamaRao BS, LaVenue AM, De Marsily G, Marietta MG. Pilot point methodology for automated calibration of an ensemble of conditionally simulated transmissivity fields: 1. Theory and computational experiments. Water Resour Res 1995;31:475–93. http://dx.doi.org/10.1029/94WR02258.
- [54] Fienen MN, Muffels CT, Hunt RJ. On constraining pilot point calibration with regularization in PEST. Ground Water 2009;47:835–44. http://dx.doi.org/10.1111/j.1745-6584.2009.00579.x.
- [55] Doherty J. Ground water model calibration using pilot points and regularization. Ground Water 2003;41:170-7. http://dx.doi.org/10.1111/j.1745-6584.2003.tb02580.x.
- [56] Doherty JE, Fienen MN, Hunt RJ. Approaches to highly parameterized inversion: pilot-point theory guidelines, and research directions. US Geological Survey Scientific Investigations, Report 2010–5168; 2010. p. 36.
- [57] Sun AY, Green R, Swenson S, Rodell M. Toward calibration of regional groundwater models using GRACE data. J Hydrol 2012;422–423:1–9. http:// dx.doi.org/10.1016/i.ihydrol.2011.10.025.
- [58] Le Ravalec M, Mouche E. Calibrating transmissivities from piezometric heads with the gradual deformation method: an application to the Culebra Dolomite unit at the waste isolation pilot plant (WIPP), New Mexico, USA. J Hydrol 2012;472–473:1–13. http://dx.doi.org/10.1016/j.jhydrol.2012.08.053.
- [59] Kazemi A, Stephen KD. Schemes for automatic history matching of reservoir modeling: a case of Nelson oilfield in UK. Pet Explor Develop 2012;39:349–61. http://dx.doi.org/10.1016/s1876-3804(12)60051-2.
- [60] Jardani A, Dupont JP, Revil A, Massei N, Fournier M, Laignel B. Geostatistical inverse modeling of the transmissivity field of a heterogeneous alluvial aquifer under tidal influence. J Hydrol 2012;472–473:287–300. http://dx.doi.org/10.1016/j.ihydrol.2012.09.031.
- [61] Doherty J. Groundwater data utilities. Part A: overview. Watermark Numer Comput 2011:67.
- [62] LaVenue AM, Pickens JF. Application of a coupled adjoint sensitivity and Kriging approach to calibrate a groundwater flow model. Water Resour Res 1992;28:1543–69. http://dx.doi.org/10.1029/92wr00208.
- [63] Doherty JE, Hunt RJ. Approaches to highly parameterized inversion: a guide to using PEST for groundwater-model calibration. US Geological Survey Scientific Investigations Report; 2010.
- [64] Wiese B, Nützmann G. Calibration of spatial aquitard distribution using hydraulic head changes and regularisation. J Hydrol 2011;408:54–66. http://dx.doi.org/10.1016/j.jihydrol.2011.07.015.
- [65] Doherty J. PEST, Model-Independent Parameter Estimation. User Manual: 5th Edition. Brisbane, Australia: Watermark Numerical, Computing; 2010.
- [66] Bhark EW, Jafarpour B, Datta-Gupta A. A generalized grid connectivity based parameterization for subsurface flow model calibration. Water Resour Res 2011:47:W06517. http://dx.doi.org/10.1029/2010wr009982.
- [67] Bayer P, Huggenberger P, Renard P, Comunian A. Three-dimensional high resolution fluvio-glacial aquifer analog: Part 1: field study. J Hydrol 2011;405:1–9. http://dx.doi.org/10.1016/i.ihydrol.2011.03.038.
- [68] Maji R, Sudicky E, Panday S, Teutsch G. Transition probability/Markov chain analyses of DNAPL source zones and plumes. Ground Water 2006;44(6):853-63. http://dx.doi.org/10.1111/ji.1745-6584.2005.00194.x.
- [69] Comunian A, Renard P, Straubhaar J, Bayer P. Three-dimensional high resolution fluvio-glacial aquifer analog Part 2: Geostatistical modeling. J Hydrol 2011;405:10–23. http://dx.doi.org/10.1016/j.jhydrol.2011.03.037.
- [70] Vesnaver A, Gualtierro B. Staggered or adapted grid for seismic tomography? The Leading Edge 2000;19:944–50.
- [71] Brauchler R, Hu R, Hu L, Jiménez S, Bayer P, Dietrich P, et al. Rapid field application of hydraulic tomography for resolving aquifer heterogeneity in unconsolidated sediments. Water Resour Res 2013;49:2013–24. http:// dx.doi.org/10.1002/wrcr.20181.
- [72] Hunt RJ, Luchette J, Schreuder WA, Rumbaugh JO, Doherty J, Tonkin MJ, et al. Using a cloud to replenish parched groundwater modeling efforts. Ground Water 2010;48:360–5. http://dx.doi.org/10.1111/j.1745-6584.2010.00699.x.
- [73] Bürger CM, Kollet S, Schumacher J, Bösel D. Introduction of a web service for cloud computing with the integrated hydrologic simulation platform ParFlow. Comput Geosci 2012;48:334–6. http://dx.doi.org/10.1016/j.cage0.2012.01.007.
- [74] Nowak W, Rubin Y, de Barros FPJ. A hypothesis-driven approach to optimize field campaigns. Water Resour Res 2012;48:W06509. http://dx.doi.org/10.1029/2011wr011016.